

Characterization of the K2-18 multi-planetary system with HARPS^{*}

A habitable zone super-Earth and discovery of a second, warm super-Earth on a non-coplanar orbit

R. Cloutier^{1,2,3}, N. Astudillo-Defru⁴, R. Doyon³, X. Bonfils⁵, J.-M. Almenara⁴, B. Benneke³, F. Bouchy⁴, X. Delfosse⁵, D. Ehrenreich⁴, T. Forveille⁵, C. Lovis⁴, M. Mayor⁴, K. Menou^{1,2}, F. Murgas⁵, F. Pepe⁴, J. Rowe³, N. C. Santos^{6,7}, S. Udry⁴, and A. Wünsche⁵

¹ Dept. of Astronomy & Astrophysics, University of Toronto, 50 St. George Street, M5S 3H4, Toronto, ON, Canada
e-mail: cloutier@astro.utoronto.ca

² Centre for Planetary Sciences, Dept. of Physical & Environmental Sciences, University of Toronto Scarborough, 1265 Military Trail, M1C 1A4, Toronto, ON, Canada

³ Institut de Recherche sur les Exoplanètes, Département de physique, Université de Montréal, CP 6128 Succ. Centre-ville, H3C 3J7, Montréal, QC, Canada

⁴ Observatoire Astronomique de l'Université de Genève, 51 chemin des Maillettes, 1290 Versoix, Switzerland

⁵ Université Grenoble Alpes, CNRS, IPAG, 38000 Grenoble, France

⁶ Instituto de Astrofísica e Ciências do Espaço, Universidade do Porto, CAUP, Rua das Estrelas, 4150-762 Porto, Portugal

⁷ Departamento de Física e Astronomia, Faculdade de Ciências, Universidade do Porto, Rua do Campo Alegre, 4169-007 Porto, Portugal

Received 12 July 2017 / Accepted 6 September 2017

ABSTRACT

Aims. The bright M2.5 dwarf K2-18 ($M_s = 0.36 M_\odot$, $R_s = 0.41 R_\odot$) at 34 pc is known to host a transiting super-Earth-sized planet orbiting within the star's habitable zone; K2-18b. Given the superlative nature of this system for studying an exoplanetary atmosphere receiving similar levels of insolation as the Earth, we aim to characterize the planet's mass which is required to interpret atmospheric properties and infer the planet's bulk composition.

Methods. We have obtained precision radial velocity measurements with the HARPS spectrograph. We then coupled those measurements with the K2 photometry to jointly model the observed radial velocity variation with planetary signals and a correlated stellar activity model based on Gaussian process regression.

Results. We measured the mass of K2-18b to be $8.0 \pm 1.9 M_\oplus$ with a bulk density of $3.3 \pm 1.2 \text{ g/cm}^3$ which may correspond to a predominantly rocky planet with a significant gaseous envelope or an ocean planet with a water mass fraction $\geq 50\%$. We also find strong evidence for a second, warm super-Earth K2-18c ($m_{p,c} \sin i_c = 7.5 \pm 1.3 M_\oplus$) at approximately nine days with a semi-major axis ~ 2.4 times smaller than the transiting K2-18b. After re-analyzing the available light curves of K2-18 we conclude that K2-18c is not detected in transit and therefore likely has an orbit that is non-coplanar with the orbit of K2-18b although only a small mutual inclination is required for K2-18c to miss a transiting configuration; $|\Delta i| \sim 1-2^\circ$. A suite of dynamical integrations are performed to numerically confirm the system's dynamical stability. By varying the simulated orbital eccentricities of the two planets, dynamical stability constraints are used as an additional prior on each planet's eccentricity posterior from which we constrain $e_b < 0.43$ and $e_c < 0.47$ at the level of 99% confidence.

Conclusions. The discovery of the inner planet K2-18c further emphasizes the prevalence of multi-planet systems around M dwarfs. The characterization of the density of K2-18b reveals that the planet likely has a thick gaseous envelope which, along with its proximity to the solar system, makes the K2-18 planetary system an interesting target for the atmospheric study of an exoplanet receiving Earth-like insolation.

Key words. techniques: radial velocities – methods: statistical – planets and satellites: detection – planets and satellites: fundamental parameters – planets and satellites: individual: K2-18

1. Introduction

Exoplanets orbiting within their host star's habitable zone may have surface temperatures that allow for the presence of liquid water on their surfaces, depending on the properties of the planetary atmosphere (Kasting et al. 1993). The presence of liquid water is a condition likely required to sustain extraterrestrial life.

This implies that habitable zone exoplanets receive comparable levels of stellar insolation to what the Earth receives from the Sun. Habitable zone exoplanets therefore represent superlative opportunities to search for life outside of the solar system via the characterization of their atmospheric structure and composition via transmission spectroscopy for transiting exoplanets.

M dwarf host stars are ideal targets to probe potentially habitable exoplanetary atmospheres (e.g. Kaltenecker et al. 2011; Rodler & López-Morales 2014). Transmission spectroscopy observations of transiting habitable zone (HZ) exoplanets around

* Table A.2 is also available at the CDS via anonymous ftp to cdsarc.u-strasbg.fr (130.79.128.5) or via <http://cdsarc.u-strasbg.fr/viz-bin/qcat?J/A+A/608/A35>

M dwarfs are favourable compared to those around Sun-like stars given the increased depth of the transit for a planet of a given size (e.g. [Stevenson et al. 2010](#); [Kreidberg et al. 2014](#)). In addition, the orbital periods corresponding to the HZ are less than those around Sun-like stars (weeks for those in the HZ of M dwarfs, compared to 12 months) thus increasing the number of accessible transit events within a given observational baseline. M dwarfs are also known to frequently host multiple small planets (typically 2.5 planets per star with $0.5 \leq r_p/R_\oplus \leq 4$ and within 200 days; [Dressing & Charbonneau 2015](#); [Gaidos et al. 2016](#)) thus enabling direct comparative planetology to be conducted on known multi-planet systems.

[Montet et al. \(2015\)](#) reported the detection of the HZ super-Earth K2-18b originally proposed in the K2 light curve analysis of [Foreman-Mackey et al. \(2015\)](#). In these studies, two transit events were observed in Campaign 1 data from the re-purposed *Kepler* spacecraft mission K2 whose field coverage only lasted for ~ 80 days. The existence of the planet was confirmed and uncertainties regarding its ephemeris were significantly reduced in [Benneke et al. \(2017](#); hereafter [B17](#)) who used follow-up transit observations with the *Spitzer* Space Telescope to detect an additional transit event. The now confirmed super-Earth K2-18b orbits an M2.5 dwarf with a period of ~ 32.9 days placing it directly within the star’s habitable zone ([Kopparapu et al. 2013](#)). The measured radius of $2.38 R_\oplus$ is suggestive of an extended H/He envelope ([Valencia et al. 2013](#); [Rogers 2015](#); [Fulton et al. 2017](#)) that may contain additional molecular species such as water and/or methane that could be detectable with the *James Webb* Space Telescope (JWST; [Beichman et al. 2014](#)). Owing to the proximity of the system (~ 34 pc, $V = 13.5$, $I = 11.7$, $K = 8.9$; [Cutri et al. 2003](#); [Zacharias et al. 2013](#)), K2-18 is truly an attractive target for characterizing the atmosphere of a HZ super-Earth with unprecedented precision in the JWST-era.

In this study we report the first measurement of the planetary mass of K2-18b using precision radial velocity measurements taken with the HARPS spectrograph. In this data we also find strong evidence for an additional planet of similar minimum mass whose orbit is interior to K2-18b but is not found to transit. In Sect. 2 we summarize the HARPS spectroscopic and K2 photometric observations used in our analysis, in Sect. 3 we analyze the periodic signals in the spectroscopic data and in Sect. 4 we discuss our various radial velocity modelling procedures. In Sect. 5 we present the results of our radial velocity analysis including the detection of a second super-Earth K2-18c in the system which we show is non-transiting and therefore is not perfectly coplanar with K2-18b in Sect. 6. Lastly we perform a dynamical analysis of the two-planet system in Sect. 7 to dynamically constrain the orbital eccentricities of the planets before concluding with a discussion in Sect. 8.

2. Observations

2.1. HARPS spectra

From April 2015 (BJD = 2457 117.5) to May 2017 (BJD = 2457 875.5), we collected 75 spectra of K2-18 (EPIC 201912552) with the high-resolution ($R = 115\,000$) HARPS spectrograph ([Mayor et al. 2003](#); [Pepe et al. 2004](#)). The majority of exposure times were fixed to 1800 s with the exception of the following six epochs whose exposure times were modified to the following reported values: 2400 s (BJD-2450 000 = 7199.503915, 7200.503114), 1200 s (BJD-2450 000 = 7204.491167), and 900 s (BJD-2450 000 = 7810.806284, 7814.760772, 7815.759421). The online HARPS

pipeline returned the extracted, wavelength-calibrated spectra ([Lovis & Pepe 2007](#)). Initial radial velocity estimates were computed from the cross-correlation of each spectrum with a numerical mask ([Baranne et al. 1996](#); [Pepe et al. 2002](#)). Using each spectrum’s initial estimate, all spectra were shifted to a common reference frame by their corresponding barycentric correction such that spectral features originating from the target star become aligned while telluric features are shifted by minus the epoch’s barycentric correction. The median combination of these shifted spectra was then used to construct a custom reference spectrum at high signal-to-noise (S/N). A telluric template was then constructed from the median combination of all residual spectra after removal of the high S/N reference stellar spectrum. The process of computing the median reference stellar spectrum was then repeated using the individual spectra with tellurics masked by the median telluric spectrum. We then computed precision radial velocities by performing a χ^2 -minimization of each spectrum with the reference spectrum ([Astudillo-Defru et al. 2015](#)). Radial velocity uncertainties were then estimated directly on the reference spectrum ([Bouchy et al. 2001](#)).

From the extracted spectra we also derived a number of activity indicators including the time series of the $H\alpha$ index which is sensitive to chromospheric activity and is computed following the definition in [Bonfils et al. \(2007\)](#). For the M dwarf K2-18 ($V = 13.5$; [Henden & Munari 2014](#)) the $H\alpha$ index is favoured over the Ca II H+K Mt. Wilson S index ([Wilson 1968](#); [Baliunas et al. 1995](#)) due to the low S/N obtained in the blue. From the S index we derived $\log R'_{HK} = -5.247 \pm 0.318$ ([Astudillo-Defru et al. 2017](#)). Additionally we derived the full width at half maximum (FWHM) and bi-sector inverse slope (BIS) shape parameters of the cross-correlation function which are modified by dark and/or bright active regions traversing the visible stellar surface. In Sect. 3 we use these ancillary time series to learn about the star’s activity simultaneously with our radial velocity measurements. All spectroscopic time series are reported in Table A.2.

2.2. K2 photometry

K2-18 was observed in long-cadence mode during Campaign 1 of the K2 mission as part of the “Targeting M dwarfs with K2” proposal (GO1053¹, PI: B. Montet). The baseline of the K2 light curve is just 80 days but provides nearly continuous coverage between June 1st, 2014 (BJD = 2456 810.5) and August 20th, 2014 (BJD = 2456 890.5).

We obtained the full de-trended light curve from the MAST² data retrieval service. As a result of the loss of two reaction wheels on-board the *Kepler* spacecraft, photometric observations from the K2 mission exhibit a reduced pointing precision, and hence photometric precision, compared to the original *Kepler* mission. Raw K2 light curves must be de-trended with the variable pointing of the spacecraft throughout the observing sequence. We selected the EVEREST reduction of the K2 light curve which performs this de-trending correction ([Luger et al. 2016](#)).

The majority of the residual photometric variability following de-trending of the light curve can be attributed to the intrinsic photometric variability of the star and two observed transits of K2-18b from [Montet et al. \(2015\)](#). Removal of the transit events provides a dataset that can be used to investigate the correlated

¹ K2-18 was also targeted in the following programmes: GO1006, GO1036, GO1050, GO1051, GO1052, GO1059, GO1063, GO1075.

² <http://archive.stsci.edu/k2/hlsp/everest/search.php>

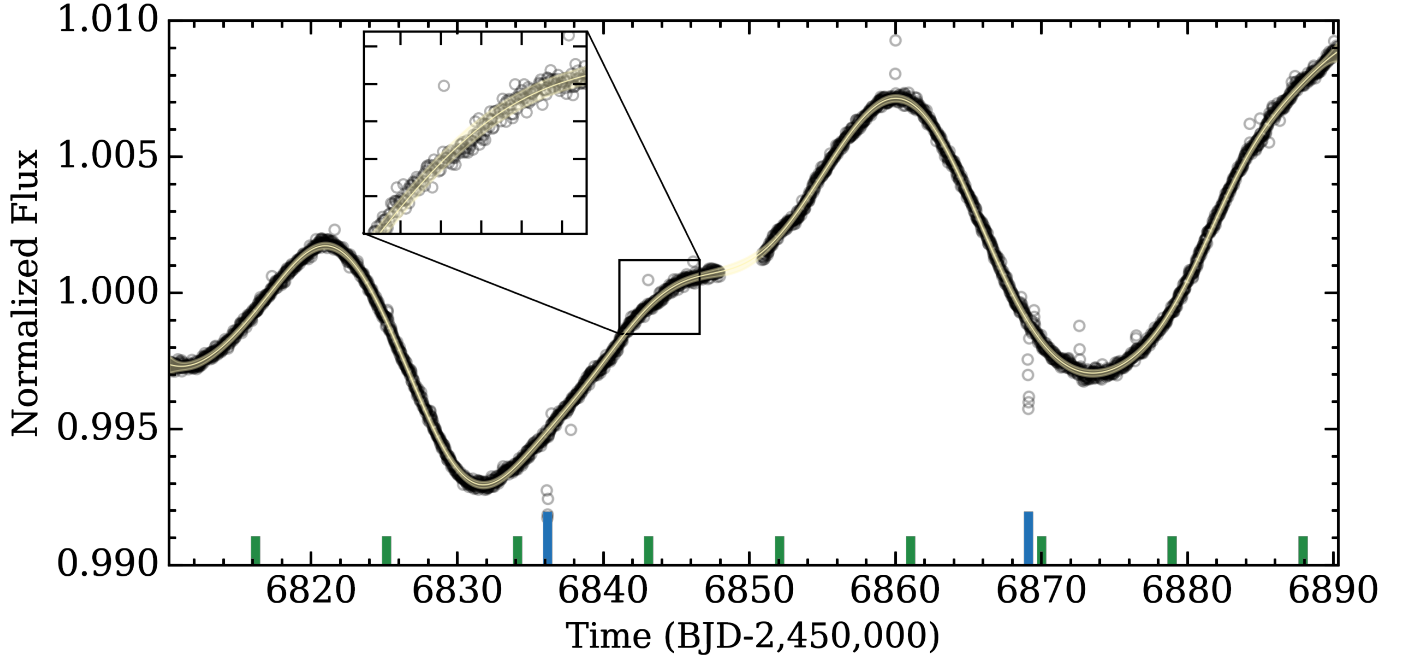


Fig. 1. K2 photometric light curve after the removal of known unphysical spurious signals. The two transits of K2-18b are highlighted by the orange blue ticks with the expected times of mid-transit for K2-18c highlighted with short green ticks (see Sect. 5). The solid yellow curve is the mean of the predictive GP distribution and the surrounding shaded regions mark its 99% confidence intervals. The upper left sub-panel is a magnified view of the highlighted region to aid in the visualization of the data and the GP fit.

photometric activity resulting from active regions traversing the visible stellar surface thus giving rise to the star’s observed photometric variability. For reference, the de-trended light curve is shown in Fig. 1 along with our Gaussian process fit to the light curve (see Sect. 4.1 for an explanation of the fit).

3. Periodogram analysis

Accurate modelling of the stellar radial velocity (RV) variations requires knowledge of the strong periodicities present in the data. These signals include contributions from both orbiting planets and from the rotation of active regions present on the stellar surface which give rise to a correlated stellar RV signal which is modulated by the stellar rotation period and/or its harmonics. In the top panel of Fig. 2 we plot the Lomb-Scargle periodogram (Scargle 1982) of the raw RVs to determine which periodicities are present at high significance, that is, those with a low false alarm probability (FAP). In all LS-periodograms we calculated FAPs via bootstrapping with replacement using 10^4 iterations and individually normalize each periodogram’s power by its standard deviation.

Two important features are detected in the LS-periodogram of the RVs. The first is a forest of peaks ranging from ~ 25 – 45 days with distinct peaks centred on both the orbital period of K2-18b ($P_b \sim 33$ days B17; FAP = 2.9%) and the approximate stellar rotation period from the K2 photometry (see Sect. 4.1 for fitting of the stellar rotation period $P_{\text{rot}} \sim 38.6$ days; FAP = 0.1%). The second important feature is a pair of closely spaced peaks at ~ 9 days (FAP < 0.01%) which because of their similar period and power likely result from a single source. This feature at approximately nine days constitutes the strongest periodic signal in the periodogram of the raw RVs and is not observed in the periodograms of any of the ancillary time series, nor in the periodogram of the window function, all of which are shown in the remaining panels of Fig. 2. The aforementioned time series

include the K2 photometry (see Fig. 1), the window function or time sampling of the HARPS observations, and four spectroscopic activity indicators: the S index, $H\alpha$ index, FWHM, and the BIS of the cross-correlation function. Together the presence of the strong ~ 9 d. signal in radial velocity and its absence elsewhere provides strong initial evidence for a second planet in the K2-18 system at ~ 9 d.

4. Joint modelling of planets and correlated RV activity

4.1. Training the GP activity model on ancillary time series

The K2 photometry of K2-18 exhibits quasi-periodic photometric variability with a semi-amplitude of ~ 0.008 mag and a rotation period of $P_{\text{rot}} \sim 38.6$ days as seen in Fig. 1. This makes K2-18 a moderately active early M dwarf in terms of its photometric variability (Newton et al. 2016) the origin of which likely results from the rotation of active regions across the projected stellar disk at or close to P_{rot} owing to the characteristically low amplitudes of differential rotation in M dwarfs (Kitchatinov & Olemskoy 2011). The observed photometric variability – or photometric activity – has a correlated manifestation in the variation of the star’s apparent radial velocity and certain spectroscopic indicators because it is a single physical process that is responsible for the activity in each time series (Aigrain et al. 2012).

In order to obtain accurate and self-consistent detections of the planetary signals in radial velocity we must model the RV activity signal of K2-18 simultaneously with our planet model. The photometric stellar rotation period of ~ 38 days (see second panel in Fig. 2) is marginally detected in the LS-periodogram of the RVs. However P_{rot} is clearly discernible by eye in the K2 light curve (Fig. 1) and has significant power in the LS-periodogram of the K2 light curve (second panel in Fig. 2) although the power is spread over a wide range of periodicities. Because of this we

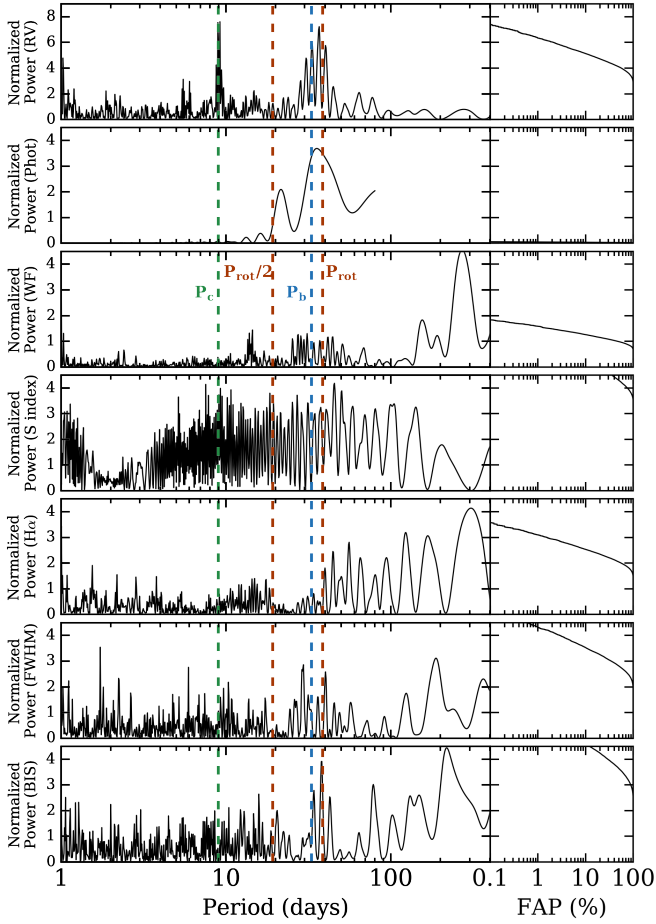


Fig. 2. *Left column (top to bottom):* Lomb-Scargle periodograms of the raw radial velocities (RV), the K2 photometry (Phot), the HARPS window function (WF), S index, $H\alpha$, full width half maximum (FWHM), and bi-sector inverse slope (BIS) time series. The orbital periods of K2-18b, K2-18c, the stellar rotation period, and its first harmonic are highlighted with vertical dashed lines. *Right column:* the false alarm probability as a function of normalized periodogram power for each time series. The FAP curve for the photometry spans very low power and is barely discernible in its subpanel. Suffice it to say that any signal with normalized power $>10^{-2}$ has a FAP $\ll 0.1\%$. The FAP curve for the S index exhibits FAP $\geq 30\%$ for all power visible on its ordinate and therefore is only visible in the upper right of its subpanel.

consider in our first model – called Model 1 – the K2 photometric light curve, less the observed transits of K2-18b, to train our RV activity model whose covariance properties are common with the observed photometric variability. However two important caveats had to be considered when adopting the K2 photometry as our training set. The first being that the baseline of the photometry spans just 80 days implying that any temporal variation whose characteristic timescale is greater than this baseline will remain unconstrained or at best weakly constrained. Secondly the K2 photometry were obtained nearly eight months prior to our HARPS observations such that any evolution in the covariance structure of the stellar activity between observing sequences from say magnetic activity cycles, would not be captured in the training set. For these reasons we also considered the BIS time series as an alternative training set in a second round of modelling called Model 2. Being contemporaneous with the RV measurements, training on the BIS time series mitigates the

two aforementioned issues. In place of the BIS we also tested training on the S index, $H\alpha$, and FWHM time series but find results consistent with training on the BIS. Following Faria et al. (2016) we also considered a joint activity + planet model but neglected any training of the activity model’s covariance structure in a third model; Model 3. Finally for comparison purposes we also considered a fourth model – called Model 4 – that neglected any contribution from stellar activity.

To implement this joint modelling procedure we followed Cloutier et al. (2017) by using a Gaussian process (GP) regression model to model the covariance between adjacent observations in our training sets where applicable (i.e. in Models 1 and 2). GP regression is an attractive method for modelling the stochastic processes that gives rise to observable RV activity signals as it is non-parametric and therefore independent of an assumed functional form of the signal. The GP prior was represented by a multi-variate Gaussian distribution of functions described by a covariance matrix $K_{ij} = k_{ij}(\theta) + \sigma_i^2 \delta_{ij}$ with a function $k_{ij}(\theta) = k(t_i, t_j, \theta)$ that parameterizes the covariance between values of the observable $\mathbf{y}(t)$ at the epochs t_i and t_j in t . The observable $\mathbf{y}(t)$ has associated uncertainties $\sigma(t)$ which were added along the diagonal of the covariance matrix K in quadrature. The set of GP hyperparameters θ are unique to the chosen covariance function $k_{ij}(\theta)$ and are solved for in the training step. After solving for the GP hyperparameters and thus obtaining a unique GP prior distribution, the GP prior conditioned on the data $\mathbf{y}(t)$ becomes the predictive distribution. The mean function of the GP predictive distribution can be evaluated at previously unseen epochs t^* using

$$\boldsymbol{\mu}(t^*) = K(t^*, t) \cdot K(t, t)^{-1} \cdot \mathbf{y}(t), \quad (1)$$

which we took to be our GP activity model of the RVs by evaluating Eq. (1) at t .

Because the stellar activity, and in particular the long-term photometric variation, is modulated by the stellar rotation period, we included a periodic term in our assumed covariance function $k_{ij}(\theta)$ with period equal to P_{rot} . We also included a radial component due to the stochastic temporal evolution of starspot lifetimes, spatial distributions, and contrasts thus forcing the covariance to not be strictly periodic. Explicitly the adopted covariance structure is parameterized by a quasi-periodic covariance kernel of the form

$$k_{i,j}(\theta) = a^2 \exp \left[-\frac{|t_i - t_j|^2}{2\lambda^2} - \Gamma^2 \sin^2 \left(\frac{\pi|t_i - t_j|}{P_{\text{GP}}} \right) \right], \quad (2)$$

which is parameterized by four hyperparameters $\theta = (a, \lambda, \Gamma, P_{\text{GP}})$: a the amplitude of the correlations, λ the exponential timescale, Γ the coherence scale of the correlations, and P_{GP} the periodic timescale of the correlations which we interpret as P_{rot} . We also included an additional scalar jitter parameter s which is added in quadrature to the diagonal elements of the covariance matrix K such that θ becomes $(a, \lambda, \Gamma, P_{\text{GP}}, s)$.

Using the Markov chain Monte-Carlo (MCMC) ensemble sampler emcee (Foreman-Mackey et al. 2013) we sample the marginalized posterior probability density functions (PDFs) of the five hyperparameters assuming uniform priors on the logarithm of each hyperparameter and maximizing the Gaussian logarithmic likelihood function

$$\ln \mathcal{L} = -\frac{1}{2} (\mathbf{y}^T K^{-1} \mathbf{y} + \ln \det K + N \ln 2\pi), \quad (3)$$

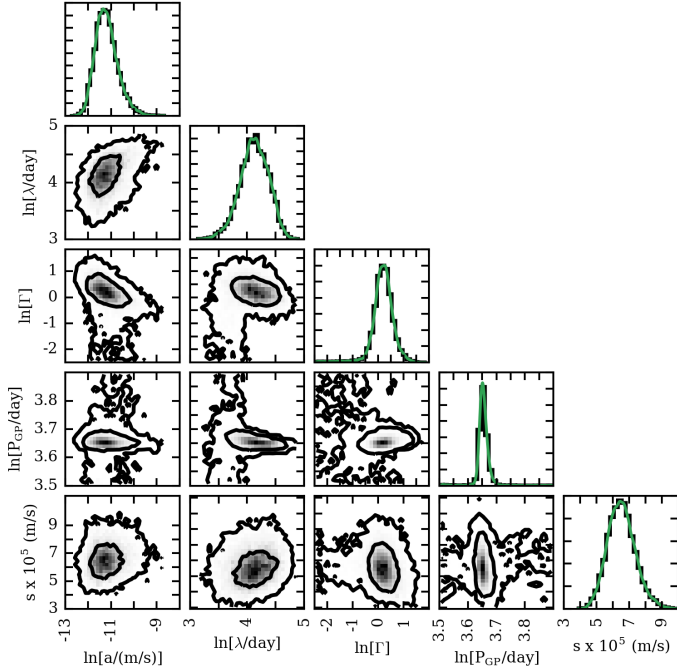


Fig. 3. Marginalized and joint posterior PDFs of the logarithmic GP hyperparameters used to model the K2 photometry shown in Fig. 1. Kernel density estimations of each model parameter’s posterior are overlaid on the histograms with solid green lines.

where \mathbf{y} is the vector of N observations in the training set. In Model 1 \mathbf{y} = the binned photometric data points³ whereas \mathbf{y} = BIS time series in Model 2.

The MCMC was initialized with 200 walkers and hyperparameter values $(a, \lambda, \Gamma, P_{GP}) = (\max(\mathbf{y} - \langle \mathbf{y} \rangle), 10^2 \text{ days}, 1, 36 \text{ days})$. We sampled the logarithmic hyperparameters up to ≈ 10 autocorrelation times to ensure adequate convergence of the chains. We also monitored the acceptance fraction for each walker and insist that it lies within 20–50%. The sampling of each hyperparameter’s marginalized posterior PDF commences following a burn-in phase of the same duration. The resulting marginalized and joint posterior PDFs are shown in Fig. 3 along with kernel density estimations of each marginalized 1D distribution. From the posterior PDF of P_{GP} we measured a stellar rotation period of $P_{\text{rot}} = 38.6^{+0.6}_{-0.4}$ days.

4.2. Joint modelling of RVs

We proceeded with modelling the RVs jointly with Keplerian solutions for both K2-18b and c plus a trained quasi-periodic GP to model the correlated RV residuals attributed to stellar activity. The marginalized posterior PDFs of the GP hyperparameters λ , Γ , and P_{GP} from training were then used as informative priors in the joint RV analysis which treat the remaining GP hyperparameters a and s as free parameters. We sampled the informative priors using the kernel density estimations of each hyperparameter’s PDF obtained during training. This methodology allows the model to learn the covariance structure of the stellar activity through observations which are independent of planetary sources and then apply that knowledge to the joint modelling of the RVs

³ Binning the K2 photometry in one day bins results in $N = 78$ compared to the 3439 unbinned photometric observations thus drastically increasing the computational efficiency of the evaluating Eq. (3) in each step of the Markov chains.

thus distinguishing between stellar activity and planet-induced Doppler shifts.

The RV modelling is again performed using *emcee*. In Models 1, 2, and 3 our RV model consisted of 16 parameters including the five GP hyperparameters discussed in Sect. 4.1, the systemic velocity of K2-18 γ_0 , the orbital periods of the two planets P , their times of inferior conjunction T_0 , their RV semi-amplitudes K , and the MCMC jump parameters $h = \sqrt{e} \cos \omega$ and $k = \sqrt{e} \sin \omega$ describing each planet’s orbital eccentricity e and argument of periastron ω . This parameterization was chosen to minimize the correlation between e and ω as well as reduce the tendency for the MCMC sampler to favour high-eccentricity solutions (Ford 2006). In Model 4 we only considered 11 model parameters as no GP activity model was included. Table 1 summarizes the adopted priors on each RV model parameter in each of the models considered in this study. We adopted non-informative priors for all Keplerian parameters other than the orbital period and time of mid-transit of K2-18b which were well-constrained by the transit light curve modelling in B17.

5. Results

5.1. Results from RV data analysis

Here we compare results from the four considered RV models. Each model contains Keplerian solutions for each of the two planets. Additionally Model 1 models the RV residuals with a quasi-periodic GP regression model that is trained on the K2 photometry in which the stellar rotation period is clearly detected (see Sect. 4.1). In this model the stellar rotation period, and hence the GP periodic term, is sufficiently distinct from the orbital period of K2-18b such that the two signals are not confused in our joint modelling and the measured semi-amplitude of K2-18b is not mis-estimated. Model 2 models the RV residuals with a quasi-periodic GP regression model that is trained on the BIS time series which is contemporaneous with the RVs. Model 3 models the RV residuals with an effectively unconstrained quasi-periodic GP and Model 4 neglects any modelling of the RV residuals therefore assuming that they are uncorrelated.

The maximum a posteriori (MAP) values of each model parameter along with the 16th and 84th percentiles of the marginalized posterior PDFs are reported in Table A.1. The marginalized and joint posterior PDFs of the model parameters used in Model 1 are shown in Fig. 4. In Sect. 5.2 we shall see that Model 1 is the best predictor of the observed RVs and therefore we only show the results from Model 1 in Fig. 4.

We emphasize that all Keplerian model parameters for the two planets are consistent at 1σ across all four models. Recall that the stellar rotation period is only well-constrained in Model 1 via the K2 photometry and yet the measured semi-amplitudes of K2-18b are consistent in each of the four models. This further demonstrates that there is minimal confusion between the RV signals at the stellar rotation period (38.6 days) and at the orbital period of K2-18b (~ 32.93 days) both of which are not distinctly detected in the periodogram of the raw RVs (see top panel of Fig. 2) but appear to be hidden within a forest of peaks spanning periodicities between ~ 25 –45 days. The consistency of all measured Keplerian parameters in each model also suggests that the RV residuals, following the removal of the two MAP Keplerian solutions, are weakly correlated because nearly identical RV solutions are obtained with and without a GP treatment of the RV residuals following the removal of our planet models. That is that K2-18 appears to be a spectroscopically

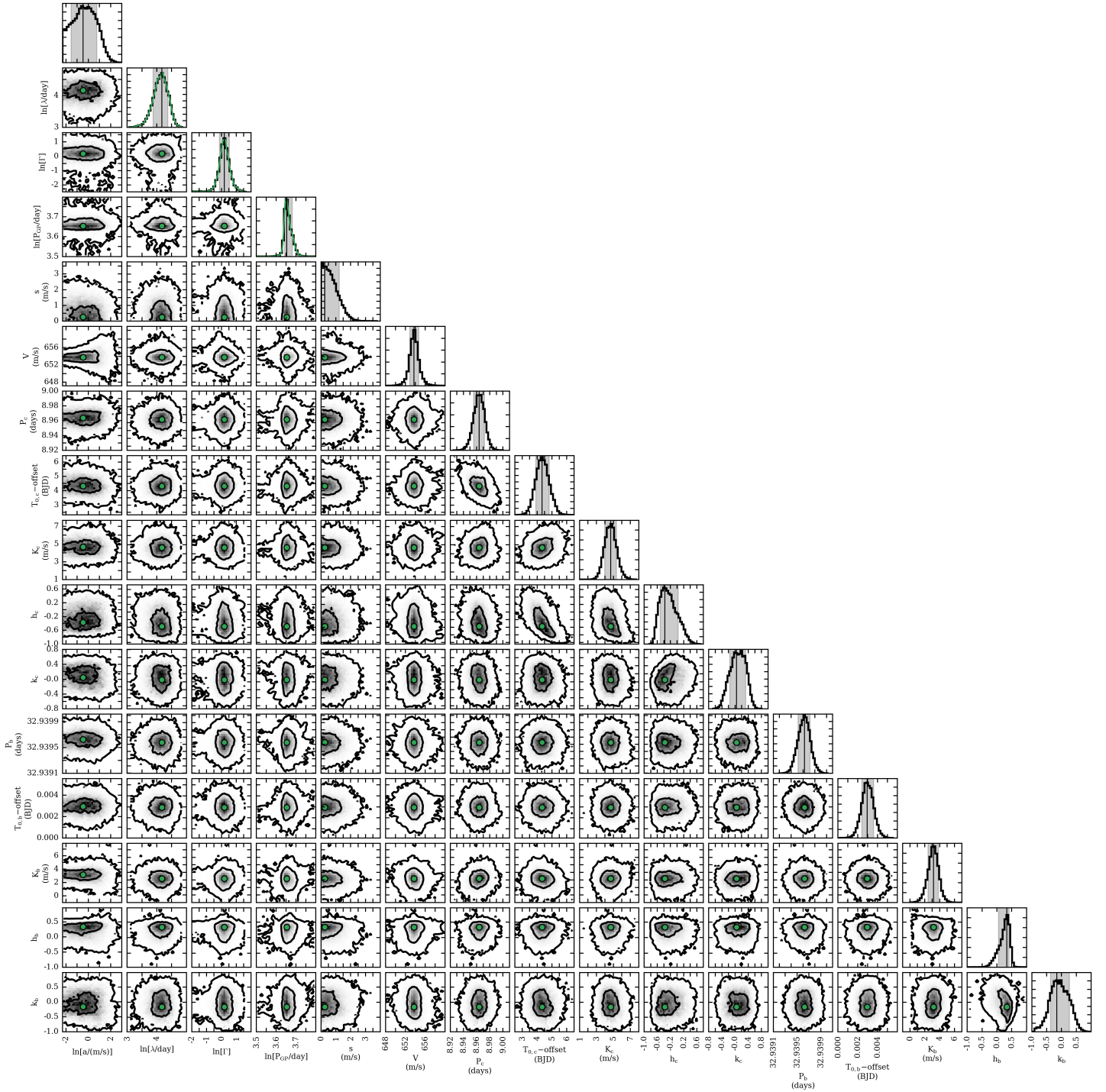


Fig. 4. The marginalized and joint posterior PDFs of the model parameters from Model 1 of the observed RVs. Model 1 of the observed RVs models the two planets with Keplerian orbital solutions and the residual RV activity signal with a GP regression model trained on the K2 photometry in Fig. 1. Kernel density estimations of the trained posteriors are shown in the histograms of the logarithmic GP hyperparameters λ , Γ , and P_{GP} (Cols. 2–4).

quiet star with the majority of its observed RV variation being attributable to planetary companions. Being spectroscopically quiet is promising for the prospect of transmission spectroscopy of K2-18b; an observation that is significantly complicated by the presence of stellar activity. The quiet nature of K2-18 is highlighted by its low measured value of $\log R'_{\text{HK}} = -5.247$.

5.2. RV model comparison

A formal model comparison between the four considered models was performed using time-series cross-validation to compute the likelihood of each model given various training and testing subsets of the observed RVs (Arlot & Celisse 2010). We split the RVs into chronological training sets with sizes ranging from

Table 1. Summary of RV models and adopted priors.

Parameter	Prior
Model 1 (2 planets + GP trained on $\mathbf{y} = \text{K2 photometry}$)	
<i>GP hyperparameters</i>	
Covariance amplitude, a [m s^{-1}]	$\mathcal{J}(0.1, 30)^*$
Exponential timescale, λ [days]	$p(\lambda \mathbf{y})$
Coherence, Γ	$p(\Gamma \mathbf{y})$
Periodic timescale, P_{GP} [days]	$p(P_{\text{GP}} \mathbf{y})$
Additive jitter, s [m s^{-1}]	$\mathcal{J}(10^{-2}, 10)$
<i>Keplerian parameters</i>	
γ_0 [m s^{-1}]	$\mathcal{U}(620, 670)$
P_b [days]	$\mathcal{N}(32.939614, 10^{-4})^\circ$
$T_{0,b}$ [BJD-2 450 000]	$\mathcal{N}(7264.39144, 6.3 \times 10^{-4})^\circ$
K_b [m s^{-1}]	$\text{mod}\mathcal{J}(1, 20)^*$
$h_b = \sqrt{e_b} \cos \omega_b$	$\mathcal{U}(-1, 1)^\ddagger$
$k_b = \sqrt{e_b} \sin \omega_b$	$\mathcal{U}(-1, 1)^\ddagger$
P_c [days]	$\mathcal{U}(8, 10)$
$T_{0,c}$ [BJD-2 450 000]	$\mathcal{U}(7259, 7269)$
K_c [m s^{-1}]	$\text{mod}\mathcal{J}(1, 20)$
$h_c = \sqrt{e_c} \cos \omega_c$	$\mathcal{U}(-1, 1)^\ddagger$
$k_c = \sqrt{e_c} \sin \omega_c$	$\mathcal{U}(-1, 1)^\ddagger$
Model 2 (2 planets + GP trained on $\mathbf{y} = \text{BIS}$)	
see Model 1	
Model 3 (2 planets + untrained GP)	
see Model 1 with the following modifications:	
In Exponential timescale, $\ln \lambda$ [days]	$\mathcal{U}(-10, 10)$
In Coherence, $\ln \Gamma$	$\mathcal{U}(-3, 3)$
In Periodic timescale, $\ln P_{\text{GP}}$ [days]	$\mathcal{U}(3.2, 4)$
Model 4 (2 planets)	
see Keplerian parameters in Model 1	

Notes. ^(*) \mathcal{J} refers to a non-informative Jeffreys prior which is scale invariant; equal probability per decade which is necessary to sample multiple orders of magnitude (Gregory 2005). ^(\circ) based on the transit light curve measurements from B17. ^(\ast) $\text{mod}\mathcal{J}(k, l) \text{ m s}^{-1}$ refers to a modified Jeffreys prior on a parameter A which behaves like a uniform prior for $A \ll$ the knee at $k \text{ m s}^{-1}$ and behaves like a Jeffreys prior at $A \gg k$ up to l . We use a modified Jeffreys prior on the RV semi-amplitudes K to sample multiple decades as a Jeffreys prior but also include $K = 0 \text{ m s}^{-1}$ which a Jeffreys prior does not (Gregory 2005). ^(\ddagger) We further insist that $e = h^2 + k^2 < 1$.

20 measurements to the size of the full dataset less one (i.e. 74 measurements). The model parameters for each of the four considered models were optimized on the training set and the likelihood of the corresponding model is evaluated on the testing set. The testing set was simply the next observation chronologically following the final observation in the training set. The resulting median likelihood and median absolute deviation for each model is reported at the bottom of Table A.1 and was used to distinguish which of our four RV models performs optimally on the prediction of unseen RV measurements and thus best fits the data without over-fitting. Through time-series cross-validation we find that Model 1 is the best predictor of the observed RVs. In the remainder of this study we consider the results

from Model 1 to be the measured values of the planets K2-18b and c.

To confirm that we have detected a second planet K2-18c in our RV data, we performed a second round of time-series cross-validation calculations. In these calculations we compared three RV models each containing 0, 1, or 2 planets. We considered K2-18b to be the lone planet in the one planet model. In each model we also considered a GP activity model that was trained on the K2 photometry as was Model 1 above. Following the same methodology as previously discussed we find median logarithmic likelihoods of $\ln \mathcal{L}_0 = -2.693 \pm 0.056$, $\ln \mathcal{L}_1 = -2.642 \pm 0.047$, and $\ln \mathcal{L}_2 = -2.566 \pm 0.026$. From this we find that $\ln \mathcal{L}_2 - \ln \mathcal{L}_1 = 0.076 \pm 0.054 > 0$ therefore arguing that the two planet model is the best predictor of unseen RV measurements and confirming that our two planet model containing both K2-18b and c is the RV model most favoured by the data.

The contributions to the observed RVs from stellar activity and each planet were depicted in Fig. 5. Together these physical models account for all significant periodicities in the observed RVs. In Fig. 5 we show the raw RVs as well as the RVs corrected for the individual RV component and compare each time series to its MAP model. In panel b we can see the relative importance of the GP activity model at modelling the RV residuals following the removal of our two planet model. Owing to the spectroscopically quiet nature of K2-18, the contribution to the observed RVs from activity is relatively small yet still holds a periodic manifestation at the stellar rotation period, albeit with a small amplitude. The residual rms following the removal of all modelled contributions is 2.89 m s^{-1} . This value is less than the median photon noise limit of the measured RVs of 3.56 m s^{-1} suggesting that we have modelled all significant RV contributions. For comparison, the residual rms achieved in Model 4, which neglects any red noise modelling following the removal of the two Keplerian solutions, is 3.16 m s^{-1} . This value is also less than the median photon noise limit suggesting that the GP regression modelling alone in Models 1, 2, and 3 does not result in over-fitting of the data.

The Model 1 MAP Keplerian orbital solutions for K2-18b and c, but with eccentricities fixed to zero, are shown in Fig. 6. Here we report circular orbital solutions given that with these data we can only place upper limits on each planet's eccentricity rather than detect it directly. The RV data are phase-folded to each planet's MAP orbital period and time of inferior conjunction and are corrected for stellar activity using the mean GP activity model trained on the K2 photometry and assuming a mean model equal to the superposition of the two MAP Keplerian solutions.

6. Searching for transits of K2-18c

From our RV analysis in Sect. 5 we derived the approximate linear ephemeris of K2-18c. We can therefore predict the passage of K2-18c at inferior conjunctions within the mostly continuous K2 photometric monitoring shown in Fig. 1. In Fig. 1 we indicate the nine such passages of K2-18c. Given the comparable minimum masses of K2-18b and c, it is reasonable to expect that the two planets also have comparable radii (recall $r_{p,b} \sim 2.38 R_\oplus$). Furthermore (Ciardi et al. 2013) argued that *Kepler* multi-planet systems with planet radii $\lesssim 3 R_\oplus$ do not exhibit a size – semi-major axis correlation such that the inner K2-18c is not expected to have undergone significant atmospheric escape compared to K2-18b. However the two 10σ transits of K2-18b are clearly discernible by-eye in the K2 photometry whereas the predicted transits of K2-18c are not. This suggests that either K2-18c is

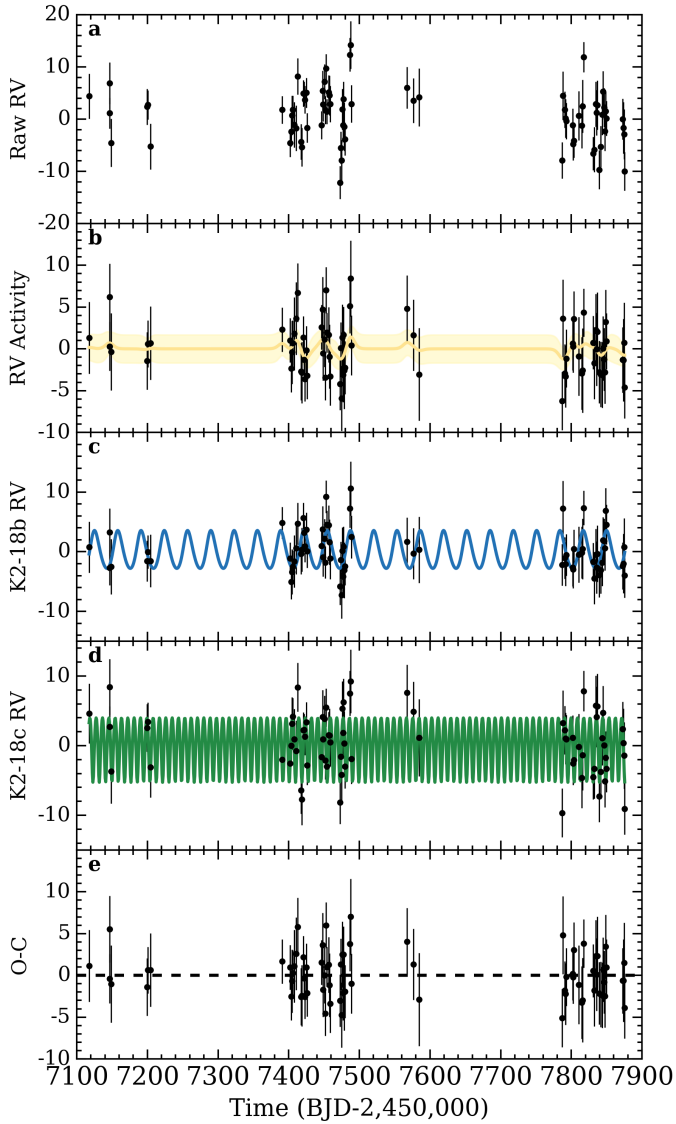


Fig. 5. Panel a: Raw RVs less the systemic velocity of K2-18. Panel b: RV contribution from stellar activity; raw RVs corrected by the MAP Keplerian orbital solutions for each detected planet. Panel c: RV contribution from K2-18b; raw RVs corrected for activity and K2-18c. Panel d: RV contribution from K2-18c; raw RVs corrected for activity and K2-18b. Panel e: the RV residuals. The solid curves in panels b, c, and d depict the mean GP activity model, and the MAP Keplerian models for K2-18b and c) respectively. The surrounding shaded region in panel b is the 68% confidence interval on the mean GP model. All RV units are in m s^{-1} .

much smaller than K2-18b such that its resulting transit depth is below the threshold for detection, or that the orbit K2-18c is mutually inclined with that of K2-18b such that it misses a transit configuration.

Here we attempt to confirm that K2-18c is indeed not transiting in the K2 light curves. To do so we perform an MCMC sampling of the K2-18c transit model parameters (P_c , $T_{0,c}$, $r_{p,c}/R_s$, a_c/R_s , and impact parameter b_c) using the K2 photometry and following the removal of the known transits of K2-18b. A quadratic limb-darkening law is assumed with fixed parameters in the *Kepler* bandpass: $a = 0.3695$ and $b = 0.3570$. These values are interpolated from the tables of Claret & Bloemen (2011)

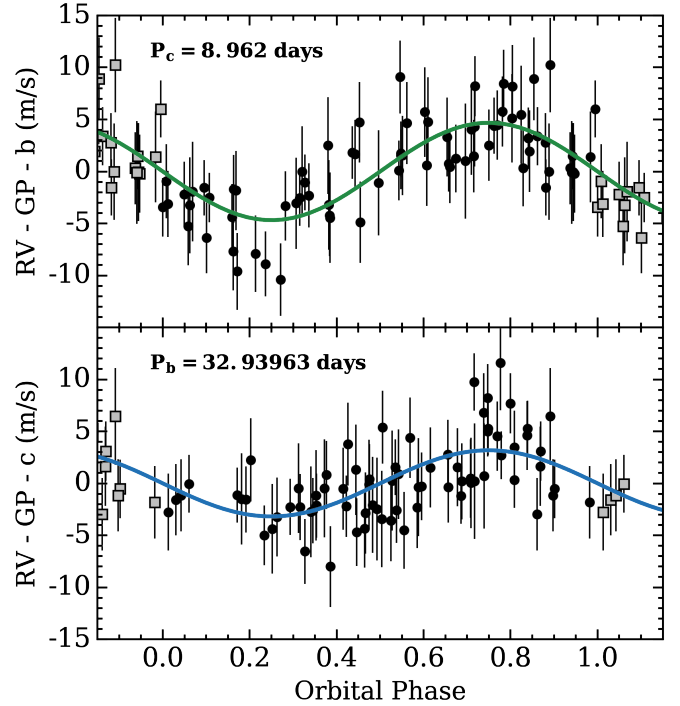


Fig. 6. Phase-folded RVs for each planet in the K2-18 planetary system (top: K2-18c and bottom: K2-18b). The RVs have been corrected for stellar activity with a quasi-periodic GP model trained on the K2 photometry. The solid curves depict the maximum a-posteriori Keplerian orbital solutions for each planet with fixed circular orbits.

based on the known K2-18 surface gravity and effective temperature. In each MCMC step we compute the corresponding transit model using the batman implementation (Kreidberg 2015) of the Mandel & Agol (2002) transit model. We assumed a circular orbit of K2-18c and adopt the same MCMC methodology utilized on the RV data in Sect. 4.2. The orbital period and time of inferior conjunction (i.e. time of mid-transit) were sampled from their joint RV posterior which maintains their apparent correlation (see Fig. 4). Priors on the scaled planet radius, and impact parameter are assumed uniform. In this way the scaled planetary radius is uncorrelated with its measured minimum mass and the impact parameter is constrained to be $|b_c| < 1$ as is required for a transit to occur.

Based on our MCMC analysis we find that the values of $r_{p,c}/R_s$ are consistent with zero, that is, no transit is detected in the K2 data. Assuming the most likely value of $R_s = 0.411 R_\odot$, we calculate a planet radius upper limit of $r_{p,c} < 0.52 R_\oplus$ at 99% confidence assuming that K2-18c is indeed transiting. However, if K2-18c were this size and transiting, albeit unknowingly due to its small size, the planet would have a bulk density of $\geq 295 \text{ g cm}^{-3}$ or $\geq 54 \rho_\oplus$; an unphysically large value given the compressibility of pure iron. Thus we conclude that K2-18c is not transiting in the K2 data and is therefore non-coplanar with K2-18b despite having a smaller orbital separation.

To visualize the data a selection of light curve models are compared to the phase-folded K2 photometry in Fig. 7. Models shown include a suite of $r_{p,c}$ values including its upper limit derived from MCMC ($0.52 R_\oplus$), $0.75 R_\oplus$, $1 R_\oplus$, and the radius of K2-18b ($2.38 R_\oplus$) which is detected at the 10σ level in the K2 photometry (Montet et al. 2015).

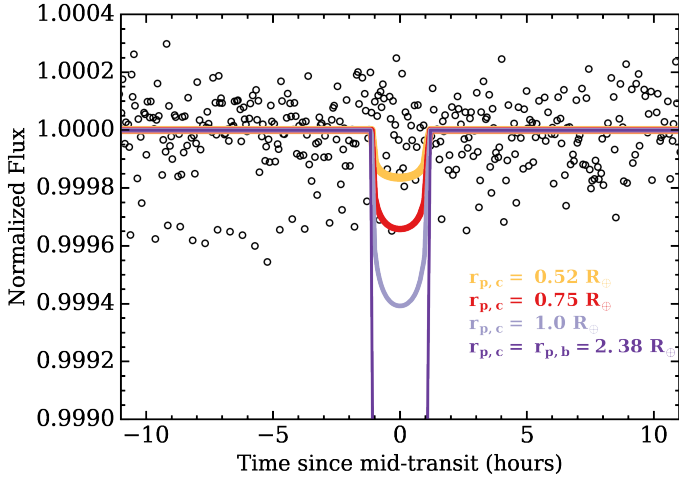


Fig. 7. K2 light curve of K2-18 phase-folded to the maximum a-posteriori orbital period and time of mid-transit of K2-18c from Model 1. Four transit light curve models are over-plotted for various illustrative values of the assumed size of K2-18c: the 99% upper limit on $r_{p,c}$ ($0.52 R_{\oplus}$), $0.75 R_{\oplus}$, $1 R_{\oplus}$, and the size of K2-18b ($2.38 R_{\oplus}$). No transit of K2-18c is detected in the data.

7. Dynamical stability and eccentricity restrictions

The non-detection of K2-18c in transit (see Sect. 6) suggests that its orbital plane is not perfectly coplanar with the outer transiting K2-18b whose semi-major axis is ~ 2.4 times greater than K2-18c's. The orbital inclination of K2-18b is $89.5785^{+0.0079}_{-0.0088}$ deg with a corresponding impact parameter of $0.601^{+0.013}_{-0.011}$ (B17). In order for the orbit of K2-18c to not pass in front of its host star its orbital inclination must be tilted either $\geq 1.41^\circ$ or $\leq -2.25^\circ$ from the orbit of K2-18b depending on which hemisphere of the stellar disk its transit chord will traverse. Such a mutual inclination is consistent with the peak in the distribution of *Kepler* multi-planet mutual inclinations (Figueira et al. 2012; Fabrycky et al. 2014). If indeed the planetary angular momentum vectors are within only a few degrees and therefore nearly aligned then we can analytically evaluate their Hill stability given estimates of their orbital eccentricities and assuming an inclination correction factor that is close to unity (Gladman 1993). If we assume the simplest case of initially circular orbits then the system is strongly Hill stable given that the two planets are currently separated by ~ 23 mutual Hill radii.

Accurate orbital eccentricities of small planets with precision radial velocities are notoriously difficult to measure. For example, the change in RV semi-amplitude of a circular K2-18b compared to an eccentricity of 0.1 is ≤ 2 cm s $^{-1}$ ($\sim 0.5\%$ of K_b) or 15 cm s $^{-1}$ ($\sim 5\%$ of K_b) for an eccentricity of 0.3. The aforementioned values are both at least an order of magnitude smaller than the characteristic RV uncertainty of the HARPS measurements presented in this work. Given that the system is Hill stable at small eccentricities we can use dynamical simulations to constrain the orbital eccentricities of the planets insisting that the system remain stable throughout its simulated evolution.

To constrain the planet eccentricities we performed a suite of 10^4 dynamical integrations wherein we sample linearly each planet's $e \in [0, 1)$. In each simulation the orbital inclination of K2-18b is drawn from $\mathcal{N}(89.5785^\circ, 0.0084^\circ)$ while the system's mutual inclination is drawn from $\mathcal{N}(\Delta i_{\min,c}, 1.5^\circ)$ such that the planet inclinations remain uncorrelated with the orbital eccentricities thus permitting an unbiased assessment of the system's stability across the Keplerian parameter space. We insist

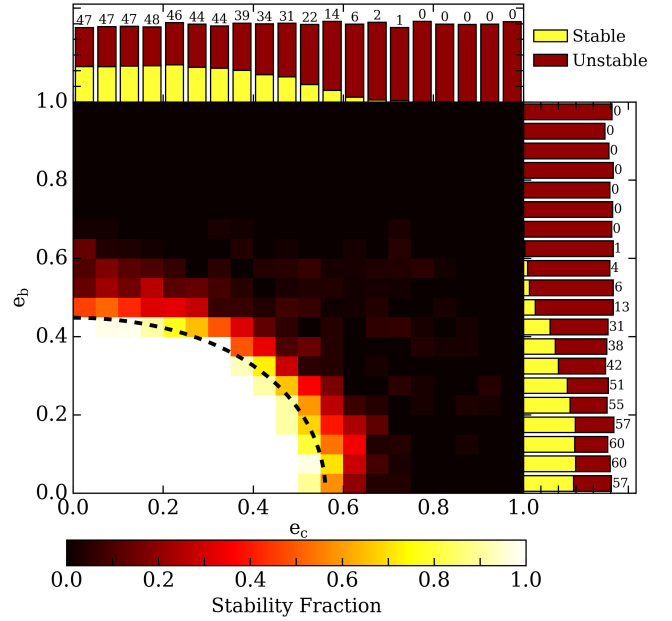


Fig. 8. Smoothed 2D map depicting the fraction of stable systems as a function of each planet's eccentricity based on a suite of dynamical integrations. The dashed black curve depicts the analytic condition for Hill stability from Gladman (1993) assuming the MAP masses and semi-major axes from Model 1 in Table A.1. 1D histograms depict the number of stable and unstable (yellow and red respectively) systems in eccentricity bins of width 0.05 and marginalized over all other dynamical parameters. The annotated numbers report each bin's stability fraction in percentages.

that K2-18c be non-transiting at the start of each simulation by setting $\Delta i_{\min,c}$ to be the minimum mutual inclination required for $|b_c| > 1$ and rejecting draws for which this is not true. The dispersion in sampled mutual inclinations is tuned such that the mode of the resulting distribution lies within $\sim 1-2^\circ$ (Fabrycky et al. 2014). Each planet's initial semi-major axis, true anomaly, and absolute mass is drawn from a Gaussian distribution with a mean value equal to the parameter's MAP value from Model 1 in Table A.1 and with standard deviations equal to its average measurement uncertainty. The stellar mass is drawn from $\mathcal{N}(0.359, 0.047) M_{\odot}$. The ascending node longitudes and arguments of periastris are both drawn from $\mathcal{U}(-\pi, \pi)$. The system is then integrated forward in time from the epoch of the first K2 photometric observation (BJD = 2 456 810.26222) for 10^6 yr using the Wisdom-Holman symplectic integrator WHFast (Rein & Tamayo 2015) implemented in the open-source REBOUND N-body package (Rein & Liu 2012). These integrations are not intended to provide a comprehensive overview of the system's dynamical stability but rather are useful to show that the system can remain stable up to at least 1 Myr and provide constraints on the planet eccentricities.

We classify stable integrations as those in which the minimum distance between the planets never becomes less than their mutual Hill radius. The fraction of stable systems as a function of each planet's eccentricity and marginalized over all other dynamical parameters is shown in Fig. 8. Strong correlations between the fraction of stable systems and dynamical parameters other than planet eccentricities was not apparent so we focus here on the effect of eccentricities only. At small eccentricities there is a large stable region wherein the fraction of systems that remain stable is $\geq 80\%$ and the system is known to be Hill stable

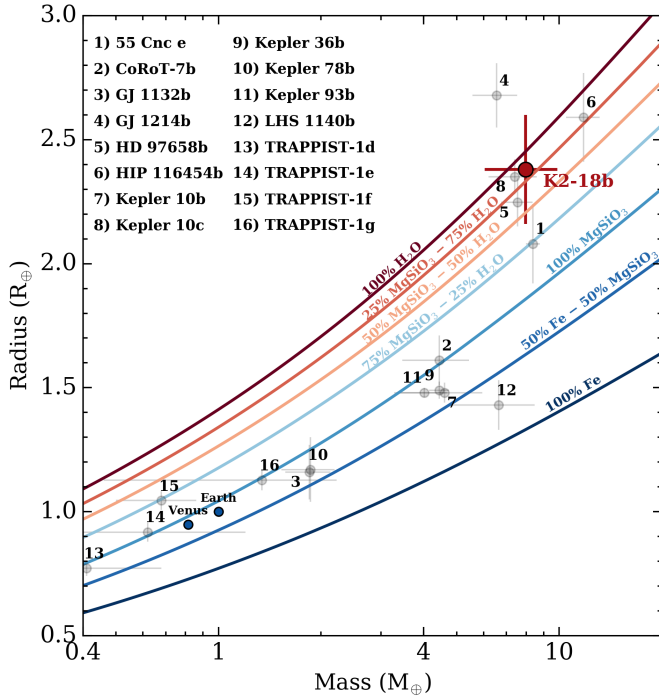


Fig. 9. K2-18b along with a sample of other small exoplanets in the planetary mass and radius space. Overlaid curves are two-component interior structure models of fully-differentiated solid planets with mass fractions annotated for each curve.

based on the analytic criterion. As we increase either planet’s eccentricity the fraction of stable systems decreases. This is also illustrated by further marginalizing over planet eccentricities and considering the one-dimensional representations of each system’s stability fraction in the histograms shown in Fig. 8.

The RV analysis discussed Sect. 5 and our dynamical simulations provide two independent methods for constraining the orbital eccentricities of the K2-18 planets. We can therefore combine these independent results by using the dynamical stability fractions shown in Fig. 8 as an additional prior on the i th planet’s derived eccentricity posterior: $e_i = h_i^2 + k_i^2$. To do this we resample each planet’s RV eccentricity posterior and accept draws with a probability equal to the stability fraction at that drawn eccentricity value ± 0.025 . This choice of bin width was varied between 0.01 and 0.1 and was found not to have a significant effect on the results. In this way numerous random samples from each planet’s RV eccentricity posterior are rejected due to the low corresponding stability fraction. This is especially true for large eccentricities wherein the system no longer satisfies the Hill stability criterion. From the modified eccentricity posteriors we can calculate the 99th percentiles and find that $e_b < 0.43$ and $e_c < 0.47$ at that confidence level. These are the eccentricity values reported in Table A.1 and represent a more stringent evaluation of each planet’s eccentricity than considering the RV data alone.

8. Discussion

With a set of 75 precision radial velocity measurements taken with the HARPS spectrograph we have obtained a robust mass measurement of the transiting HZ super-Earth K2-18b and detected a second super-Earth K2-18c. The orbit of the newly discovered K2-18c lies interior to that of K2-18b and yet the planet is non-transiting. This implies that the orbital planes of the planets are mutually inclined. In order for K2-18c to not be

seen in-transit the planetary system requires a mutual inclination of just $\geq 1.4^\circ$ which is consistent with the observed distribution of mutually inclined multi-planet systems (Figueira et al. 2012; Fabrycky et al. 2014). Dynamical simulations of the system revealed that the oscillation timescale of the planets’ orbital inclinations is $O(10^6 \text{ yr})$ suggesting that it may take many years before K2-18c reaches a transiting configuration. Although exactly how long depends sensitivity on its current inclination which remains unknown. The discovery of RV planets in transiting M dwarf planetary systems further emphasizes the prevalence of multiple Earth to super-Earth-sized planets around nearby M dwarfs and that these additional planets can be uncovered with moderate RV follow-up (Cloutier et al. 2017). Multi-planet systems such as K2-18 provide unique opportunities to study planet formation processes around M dwarfs via direct comparative planetology.

The presence of a second planet in the K2-18 transiting system will result in mutual planetary interactions thus making the orbit of K2-18b non-Keplerian and possibly resulting in an observable transit timing variation (TTV). Assuming a mutual inclination of K2-18c that just misses a transiting configuration, we estimate the expected TTVs of K2-18b using the TTVFaster package (Deck et al. 2014; Agol & Deck 2016). We adopted the maximum a-posteriori masses and orbital periods of the two planets from Model 1 and uniformly sample their eccentricities up to the 99% upper limits reported in Table A.1. The remaining orbital parameters of the planets that are unconstrained by the RV data are sampled uniformly between 0 and 2π . We find a maximum TTV for K2-18b of $\sim 40 \text{ s}$ which is slightly less than, but of the same order as the uncertainty in its measured time of mid-transit ($\sim 50 \text{ s}$; B17). Thus with photometric monitoring of at least comparable quality to the K2 photometry shown in Fig. 1, detecting TTVs in the K2-18 multi-planet system is unlikely to provide any significant new insight into the nature of the system. Indeed no significant TTVs were observed in the *Spitzer* light curves from B17.

With our measured mass of K2-18b the planet joins a select group of HZ planets with constraints on both its mass and radius. This represents a significant step towards searching for potentially habitable planets around stars earlier than $\sim M4$ (Dittmann et al. 2017). With its maximum a posteriori mass of $7.96 \pm 1.91 M_\oplus$ the bulk density of K2-18b ($\rho_{p,b} = 3.3 \pm 1.2 \text{ g cm}^{-3}$) lies between that of an Earth-like rocky planet and a low density Neptune-like planet. The planet is therefore likely too large to be a terrestrial Earth-like planet (Valencia et al. 2007; Fulton et al. 2017). Including K2-18b on the exoplanet mass-radius diagram in Fig. 9 we find that the internal structure of K2-18b is consistent with a range of two-component solid-planet models (Zeng & Sasselov 2013) owing to the uncertainty in its measured radius and mass which is at the level of $\sim 24\%$. In particular, the 1σ lower mass limit of K2-18b permits it to be a complete “water world” even though its upper mass limit is consistent with a largely rocky interior surrounded by a significant mass fraction of water ice. In this parameter space the physical parameters of K2-18b are most similar to the super-Earths HD 97658b (Van Grootel et al. 2014) and *Kepler* 10c (Dumusque et al. 2014; Rajpaul et al. 2017) despite receiving ~ 65 and ~ 24 times less insolation than those two planets respectively. Furthermore K2-18b is of a similar mass to the habitable zone planet LHS 1140b (Dittmann et al. 2017) and receives a comparable level of insolation despite being ~ 1.6 times larger than LHS 1140b. Analyzing the mass-radius relationship of these small planets over a range of equilibrium temperatures is a critical step towards understanding which of these systems

have retained significant atmospheric content thus making them more suitable to extraterrestrial life.

Distinguishing between K2-18b as a pure water-world or a scaled-up Earth with a significant gaseous envelope will likely require transmission spectroscopy follow-up observations either with high-resolution spectrographs from the ground or from space with JWST. With $J = 9.8$, $H = 9.1$, and $K = 8.9$ (Cutri et al. 2003), we stress that K2-18 is currently the second brightest M dwarf with a transiting habitable zone planet behind the recently discovered LHS 1140b. In the coming years the sample of habitable zone M dwarf planets is expected to increase dramatically following the launch of TESS (Ricker et al. 2014), although the majority of TESS planets will be more distant than LHS 1140 (Sullivan et al. 2015).

Considering the prospect of observational follow-up of K2-18b in transmission spectroscopy, if we consider an atmosphere that is cloud-free and dominated by hydrogen, then spectral features from well-mixed near-IR absorbing species such as water would have amplitudes of $\Delta F/F \sim 10Hr_p/R_s^2 \sim 230$ ppm where $H = k_B T_{eq}/\mu g$ is the atmospheric scale height, T_{eq} is the planet's equilibrium temperature set by the stellar insolation, μ is the mean molecular weight of the atmosphere, and g is the surface gravity (Miller-Ricci et al. 2009; Kaltenegger & Traub 2009). If instead the atmosphere is dominated by heavier elements, similar Earth's (e.g. $N_2 + O_2$, $\mu = 29$), then the transmission signal will be significantly smaller (~ 10 ppm) though potentially still detectable with JWST with several visits. Because of the brightness of its host star and the low bulk density of K2-18b, the system offers a unique opportunity to study super-Earth atmospheres receiving Earth-like insolation in the JWST-era.

Acknowledgements. R.C. is partially supported in this work by the National Science and Engineering Research Council of Canada and the Institute for Research on Exoplanets. R.C. would like to thank Dan Tamayo for his useful discussions regarding the dynamical simulations presented in this work and their interpretation. X.B., X.D., and T.F. acknowledge the support of CNRS/PNP (Programme national de planétologie). D.E. acknowledges support from the National Centre for Competence in Research "Planets" of the Swiss National Science Foundation (SNSF) and from the European Research Council (ERC) under the European Union's Horizon 2020 research and innovation programme (grant agreement No. 724427). X.B., J.M.A. and A.W. acknowledge funding from the European Research Council under the ERC Grant Agreement No. 337591-ExTrA. N.C.S. acknowledges support from Fundação para a Ciência e a Tecnologia (FCT) through national funds and from FEDER through COMPETE2020 by the following grants: UID/FIS/04434/2013 & POCI-01-0145-FEDER-007672 and PTDC/FIS-AST/1526/2014 & POCI-01-0145-FEDER-016886. NCS also acknowledges the support from FCT through Investigador FCT contract IF/00169/2012/CP0150/CT0002. Some of the data presented in this paper were obtained from the Mikulski Archive for Space Telescopes (MAST). STScI is operated by the Association of Universities for Research in Astronomy, Inc., under NASA contract NAS5-26555. Support for MAST for non-HST data is provided by the NASA Office of Space Science via grant NNX09AF08G and by other grants and contracts.

References

Agol, E., & Deck, K. 2016, *ApJ*, 818, 177
Aigrain, S., Pont, F., & Zucker, S. 2012, *MNRAS*, 419, 3147

Arlot, S., & Celisse, A. 2010, *Statist. Surv.*, 4, 40
Astudillo-Defru, N., Bonfils, X., Delfosse, X., et al. 2015, *A&A*, 575, A119
Astudillo-Defru, N., Delfosse, X., Bonfils, X., et al. 2017, *A&A*, 600, A13
Baliunas, S. L., Donahue, R. A., Soon, W. H., et al. 1995, *ApJ*, 438, 269
Baranne, A., Queloz, D., Mayor, M., et al. 1996, *A&AS*, 119, 373
Beichman, C., Benneke, B., Knutson, H., et al. 2014, *PASP*, 126, 1134
Benneke, B., Werner, M., Petigura, E., et al. 2017, *ApJ*, 834, 187
Bonfils, X., Mayor, M., Delfosse, X., et al. 2007, *A&A*, 474, 293
Bouchy, F., Pepe, F., & Queloz, D. 2001, *A&A*, 374, 733
Ciardi, D. R., Fabrycky, D. C., Ford, E. B., et al. 2013, *ApJ*, 763, 41
Claret, A., & Bloemen, S. 2011, *A&A*, 529, A75
Cloutier, R., Doyon, R., Menou, K., et al. 2017, *AJ*, 153, 9
Cutri, R. M., Skrutskie, M. F., van Dyk, S., et al. 2003, 2MASS All Sky Catalog of point sources
Deck, K. M., Agol, E., Holman, M. J., & Nesvorný, D. 2014, *ApJ*, 787, 132
Dittmann, J. A., Irwin, J. M., Charbonneau, D., et al. 2017, *Nature*, 544, 333
Dressing, C. D., & Charbonneau, D. 2015, *ApJ*, 807, 45
Dumusque, X., Bonomo, A. S., Haywood, R. D., et al. 2014, *ApJ*, 789, 154
Fabrycky, D. C., Lissauer, J. J., Ragozzine, D., et al. 2014, *ApJ*, 790, 146
Faria, J. P., Haywood, R. D., Brewer, B. J., et al. 2016, *A&A*, 588, A31
Figueira, P., Marmier, M., Boué, G., et al. 2012, *A&A*, 541, A139
Ford, E. B. 2006, *ApJ*, 642, 505
Foreman-Mackey, D., Hogg, D. W., Lang, D., & Goodman, J. 2013, *PASP*, 125, 306
Foreman-Mackey, D., Montet, B. T., Hogg, D. W., et al. 2015, *ApJ*, 806, 215
Fulton, B. J., Petigura, E. A., Howard, A. W., et al. 2017, *AJ*, 154, 109
Gaidos, E., Mann, A. W., Kraus, A. L., & Ireland, M. 2016, *MNRAS*, 457, 2877
Gladman, B. 1993, *Icarus*, 106, 247
Gregory, P. C. 2005, *ApJ*, 631, 1198
Henden, A., & Munari, U. 2014, *Contributions of the Astronomical Observatory Skalnaté Pleso*, 43, 518
Kaltenegger, L., & Traub, W. A. 2009, *ApJ*, 698, 519
Kaltenegger, L., Segura, A., & Mohanty, S. 2011, *ApJ*, 733, 35
Kasting, J. F., Whitmire, D. P., & Reynolds, R. T. 1993, *Icarus*, 101, 108
Kitchatinov, L. L., & Olemko, S. V. 2011, *MNRAS*, 411, 1059
Kopparapu, R. K., Ramirez, R., Kasting, J. F., et al. 2013, *ApJ*, 765, 131
Kreidberg, L. 2015, *PASP*, 127, 1161
Kreidberg, L., Bean, J. L., Désert, J.-M., et al. 2014, *Nature*, 505, 69
Lovis, C., & Pepe, F. 2007, *A&A*, 468, 1115
Luger, R., Agol, E., Kruse, E., et al. 2016, *AJ*, 152, 100
Mandel, K., & Agol, E. 2002, *ApJ*, 580, L171
Mayor, M., Pepe, F., Queloz, D., et al. 2003, *The Messenger*, 114, 20
Miller-Ricci, E., Seager, S., & Sasselov, D. 2009, *ApJ*, 690, 1056
Montet, B. T., Morton, T. D., Foreman-Mackey, D., et al. 2015, *ApJ*, 809, 25
Newton, E. R., Irwin, J., Charbonneau, D., et al. 2016, *ApJ*, 821, 93
Pepe, F., Mayor, M., Galland, F., et al. 2002, *A&A*, 388, 632
Pepe, F., Mayor, M., Queloz, D., et al. 2004, *A&A*, 423, 385
Rajpaul, V., Buchhave, L. A., & Aigrain, S. 2017, *MNRAS*, 471, L125
Rein, H., & Liu, S.-F. 2012, *A&A*, 537, A128
Rein, H., & Tamayo, D. 2015, *MNRAS*, 452, 376
Ricker, G. R., Winn, J. N., Vanderspek, R., et al. 2014, in *Space Telescopes and Instrumentation 2014: Optical, Infrared, and Millimeter Wave*, Proc. SPIE, 9143, 914320
Rodler, F., & López-Morales, M. 2014, *ApJ*, 781, 54
Rogers, L. A. 2015, *ApJ*, 801, 41
Scargle, J. D. 1982, *ApJ*, 263, 835
Stevenson, K. B., Harrington, J., Nymeyer, S., et al. 2010, *Nature*, 464, 1161
Sullivan, P. W., Winn, J. N., Berta-Thompson, Z. K., et al. 2015, *ApJ*, 809, 77
Valencia, D., Sasselov, D. D., & O'Connell, R. J. 2007, *ApJ*, 665, 1413
Valencia, D., Guillot, T., Parmentier, V., & Freedman, R. S. 2013, *ApJ*, 775, 10
Van Grootel, V., Gillon, M., Valencia, D., et al. 2014, *ApJ*, 786, 2
Wilson, O. C. 1968, *ApJ*, 153, 221
Zacharias, N., Finch, C. T., Girard, T. M., et al. 2013, *AJ*, 145, 44
Zeng, L., & Sasselov, D. 2013, *PASP*, 125, 227

Appendix A: Additional tables

Table A.1. Model parameters.

Parameter	Maximum a posteriori values with 16th and 84th percentiles			
	Model 1	Model 2	Model 3	Model 4
<i>Stellar parameters</i>				
2MASS Photometry	$J = 9.763 \pm 0.028$, $H = 9.135 \pm 0.026$, $K_s = 8.899 \pm 0.019$			
Stellar mass, M_s [M_\odot]	0.359 ± 0.047			
Stellar radius, R_s [R_\odot]	0.411 ± 0.038			
Effective temperature, T_{eff} [K]	3457 ± 39			
Distance, d [pc]	34 ± 4			
Rotation period, P_{rot} [days]	$38.6^{+0.6}_{-0.4}$			
Systemic velocity, γ_0 [m s^{-1}]	$653.7 \pm 0.9^*$			
<i>GP hyperparameters</i>				
Covariance amplitude, a [m s^{-1}]		N.S. ^(c)	N.S.	–
Exponential timescale, λ [days]		N.S.	N.S.	–
Coherence, Γ		N.S.	N.S.	–
Periodic timescale, P_{GP} [days]		N.S.	N.S.	–
Additive jitter, s [m s^{-1}]		$0.45^{+0.85}_{-0.23}$	$0.22^{+1.09}_{-0.04}$	–
<i>K2-18c</i>				
Period, P_c [days]	8.962 ± 0.008	8.964 ± 0.010	8.965 ± 0.010	$8.966^{+0.005}_{-0.010}$
Time of inferior conjunction, $T_{0,c}$ [BJD-2 450 000]	7264.55 ± 0.46	7264.55 ± 0.51	$7264.49^{+0.58}_{-0.45}$	$7264.48^{+0.61}_{-0.31}$
Radial velocity semi-amplitude, K_c [m s^{-1}]	4.63 ± 0.72	$4.74^{+0.71}_{-0.98}$	4.52 ± 0.82	$4.63^{+0.82}_{-0.58}$
$h_c = \sqrt{e_c} \cos \omega_c$	$-0.37^{+0.41}_{-0.35}$	$-0.46^{+0.45}_{-0.35}$	$-0.39^{+0.51}_{-0.39}$	$-0.51^{+0.57}_{-0.39}$
$k_c = \sqrt{e_c} \sin \omega_c$	$0.05^{+0.38}_{-0.21}$	$-0.04^{+0.35}_{-0.13}$	$0.00^{+0.39}_{-0.17}$	$0.01^{+0.39}_{-0.17}$
Semi-major axis, a_c [AU]	0.060 ± 0.003	0.060 ± 0.003	0.060 ± 0.003	0.060 ± 0.003
Eccentricity, e_c	$< 0.47^*$	–	–	–
Minimum planet mass, $m_{p,c} \sin i_c$ [M_\oplus]	7.51 ± 1.33	$7.68^{+1.33}_{-1.72}$	7.33 ± 1.48	$7.51^{+1.48}_{-1.15}$
Equilibrium temperature, $T_{\text{eq},c}$ [K]		363 ± 14	363 ± 14	363 ± 14
Bond albedo of 0.3				
<i>K2-18b</i>				
Period, P_b [days]	$32.93963 \pm 1.0 \times 10^{-4}$	$32.93962 \pm 1.1 \times 10^{-4}$	$32.93961 \pm 1.0 \times 10^{-4}$	$32.93960 \pm 9.3 \times 10^{-5}$
Time of inferior conjunction, $T_{0,b}$ [BJD-2 450 000]	$7264.39157 \pm 5.9 \times 10^{-4}$	$7264.39133 \pm 6.4 \times 10^{-4}$	$7264.39155^{+0.0006}_{-0.0008}$	$7264.39135^{+0.0007}_{-0.0005}$
Radial velocity semi-amplitude, K_b [m s^{-1}]	3.18 ± 0.71	$3.29^{+0.71}_{-0.66}$	$3.26^{+0.65}_{-0.67}$	$3.25^{+0.60}_{-0.66}$
$h_b = \sqrt{e_b} \cos \omega_b$	$0.33^{+0.08}_{-0.28}$	$0.35^{+0.08}_{-0.30}$	$0.31^{+0.07}_{-0.37}$	$0.32^{+0.06}_{-0.27}$
$k_b = \sqrt{e_b} \sin \omega_b$	$-0.16^{+0.42}_{-0.21}$	$-0.16^{+0.42}_{-0.19}$	$-0.10^{+0.41}_{-0.25}$	$-0.11^{+0.31}_{-0.22}$
Semi-major axis, a_b [AU]	0.143 ± 0.006	0.143 ± 0.006	0.143 ± 0.006	0.143 ± 0.006
Eccentricity, e_b	$< 0.43^*$	–	–	–
Planet mass, $m_{p,b}$ [M_\oplus] [†]	7.96 ± 1.91	$8.23^{+1.92}_{-1.76}$	$8.16^{+1.73}_{-2.24}$	$8.13^{+1.66}_{-1.25}$
Planet density, $\rho_{p,b}$ [g cm^{-3}] [‡]	3.3 ± 1.2	$3.4^{+1.2}_{-1.2}$	$3.4^{+1.2}_{-1.3}$	$3.3^{+1.2}_{-1.0}$
Surface gravity, g [m s^{-2}] [‡]	14.0 ± 4.3	$14.5^{+4.3}_{-4.3}$	$14.4^{+4.3}_{-3.4}$	$14.3^{+4.3}_{-3.3}$
Escape velocity, $v_{\text{esc},b}$ [km s^{-1}] [‡]	20.6 ± 2.7	$20.9^{+2.6}_{-2.4}$	$20.9^{+2.4}_{-3.0}$	$20.8^{+2.3}_{-1.9}$
Equilibrium temperature, $T_{\text{eq},b}$ [K]		235 ± 9	235 ± 9	235 ± 9
Bond albedo of 0.3				
<i>Model diagnostics</i>				
Median $\ln \mathcal{L}$ from Cross-Validation	-1.462 ± 0.013	-1.574 ± 0.017	-1.600 ± 0.018	-1.548 ± 0.017
$\ln \mathcal{L}_1 - \ln \mathcal{L}_i$	0	0.112 ± 0.021	0.138 ± 0.022	0.086 ± 0.021

Notes. ^(c) from the Model 1 RV modelling. ^(†) N.S. stands for “no solution” and occurs when the parameter’s marginalized posterior PDF is unconstrained by the data. ^(*) upper limit based on the 99% confidence interval from the RV data analysis and conditioned on the dynamical stability constraints from Sect. 7. ^(‡) assuming the measured orbital inclination of K2-18b from B17; $i_b = 89.5785^{+0.0079}_{-0.0088}$ deg. ^(§) assuming the measured radius of K2-18b from B17; $r_{p,b} = 2.38 \pm 0.22 R_\oplus$, $M_\oplus = 1.988499 \times 10^{30}$ kg, $R_\oplus = 6.955 \times 10^6$ m, $M_\oplus = 6.045898 \times 10^{24}$ kg, $R_\oplus = 6.378137 \times 10^6$ m.

Table A.2. HARPS time series.

BJD-2450000	RV [m s ⁻¹]	σ RV [m s ⁻¹]	S index	H α	FWHM	BIS
7117.565870	658.15	4.30	0.551	0.06337	3.050	9.397
7146.526948	654.90	2.94	0.851	0.06646	3.068	-3.008
7146.646070	660.66	3.98	0.537	0.06850	3.079	-6.150
7148.518851	649.21	4.62	0.973	0.06667	3.071	8.583
7199.503915	656.11	3.43	0.558	0.06597	3.090	16.922
7200.503114	656.48	2.79	0.290	0.06625	3.080	19.343
7204.491167	648.52	4.38	0.368	0.06409	3.076	-10.068
7390.845075	655.54	2.65	1.040	0.06721	3.106	-0.196
7401.779223	649.19	2.66	0.960	0.06640	3.105	1.064
7403.826871	651.38	2.87	1.287	0.06598	3.106	5.332
7404.814521	654.49	3.78	1.410	0.06679	3.095	6.633
7405.789149	655.54	2.71	1.066	0.06644	3.106	7.934
7407.773473	652.66	4.36	-	0.06680	3.048	0.311
7410.791609	651.99	4.35	1.296	0.07166	3.114	-2.344
7412.810195	661.94	3.50	0.677	0.06618	3.094	-8.771
7417.787334	649.38	3.41	0.724	0.06615	3.092	7.447
7418.799229	648.38	3.67	1.402	0.06842	3.100	2.274
7420.791577	658.68	2.54	1.170	0.06738	3.099	11.285
7421.794046	658.62	2.30	1.509	0.07463	3.099	11.310
7422.781258	657.47	2.66	0.986	0.06505	3.104	7.032
7424.777426	658.79	2.86	0.924	0.06642	3.104	5.314
7425.850669	652.07	2.81	0.871	0.06636	3.088	-0.471
7446.704487	652.60	2.67	0.933	0.06481	3.108	1.511
7447.830725	659.17	3.87	0.862	0.06539	3.085	0.282
7448.686909	656.59	3.26	0.713	0.06470	3.098	0.282
7450.675147	660.91	3.33	0.917	0.06521	3.102	-8.218
7451.677499	655.48	2.70	1.063	0.06575	3.111	-5.083
7452.695705	663.48	2.75	1.112	0.06532	3.093	1.667
7453.701988	655.18	2.38	1.038	0.06689	3.104	10.356
7456.704230	658.87	3.31	0.887	0.06586	3.111	-17.835
7457.683261	658.28	3.81	1.010	0.06615	3.101	12.792
7458.660021	656.62	3.47	1.404	0.06634	3.099	9.160
7472.784787	641.61	3.12	1.058	0.06653	3.094	-1.001
7473.684129	648.26	3.08	0.908	0.06529	3.096	-1.293
7474.737446	645.84	3.90	0.783	0.06621	3.085	-6.991
7475.698658	655.63	3.94	0.331	0.06647	3.094	-0.455
7476.707703	652.59	3.26	0.983	0.06517	3.091	-0.985
7477.674398	657.56	3.37	0.816	0.06554	3.100	-4.990
7478.631994	652.31	4.64	0.682	0.06713	3.093	-9.857
7479.737617	649.94	3.17	1.116	0.06541	3.086	-9.996
7486.661319	666.10	3.24	1.168	0.06527	3.096	-10.681
7487.617699	667.97	4.55	0.573	0.06504	3.091	-0.986
7488.670507	656.68	3.56	0.922	0.06431	3.086	-8.201
7567.516862	659.76	4.00	0.993	0.06530	3.096	10.014
7576.473152	657.32	4.27	0.989	0.06587	3.115	7.131
7584.477527	657.94	5.55	0.725	0.06563	3.080	16.445
7786.842858	645.83	3.49	1.146	0.06430	3.093	-1.668
7787.825672	658.25	4.66	0.944	0.06581	3.092	5.481
7790.828228	655.56	3.49	1.092	0.06500	3.088	1.878
7791.843445	653.87	3.70	0.700	0.06414	3.093	-3.719
7792.815105	653.38	3.47	0.893	0.06861	3.083	6.408
7801.827514	652.57	3.18	0.812	0.06518	3.094	12.389
7802.790293	648.98	3.14	0.860	0.06504	3.094	-3.525
7803.809311	649.61	3.27	0.926	0.06616	3.091	18.332
7810.806284	654.41	4.71	0.905	0.06593	3.098	6.496
7814.760772	652.53	4.35	-	0.06632	3.098	-0.563
7815.759421	656.22	5.06	-	0.06536	3.086	15.990
7817.748614	665.63	2.89	0.998	0.06423	3.103	7.162
7830.668729	647.15	3.18	0.866	0.06476	3.084	-1.992
7832.659387	647.89	4.31	1.029	0.06292	3.079	14.048
7834.636450	656.64	4.31	1.025	0.06407	3.091	9.870
7835.596293	654.97	4.36	1.004	0.06308	3.093	11.521
7836.626075	656.46	4.71	0.792	0.06491	3.093	-2.004
7839.650934	644.07	3.74	0.774	0.06437	3.076	5.253
7841.638147	648.49	3.92	0.810	0.06487	3.089	0.543
7843.648062	654.65	3.92	0.408	0.06404	3.090	12.825
7844.626814	659.07	3.85	0.722	0.06417	3.087	1.584
7846.692642	655.96	3.75	0.923	0.06435	3.086	5.210
7847.693240	651.46	3.77	0.903	0.06363	3.094	8.538
7848.677241	655.24	3.82	0.848	0.06445	3.102	1.280
7849.696944	653.92	3.34	0.853	0.06440	3.082	9.616
7872.656844	653.72	3.92	0.913	0.06371	3.082	-5.325
7873.525484	652.07	4.95	0.813	0.06478	3.094	13.489
7874.671695	650.86	4.80	0.886	0.06543	3.088	1.857
7875.596914	643.77	3.69	0.913	0.06467	3.077	5.739